J Mater Sci (2007) 42:4233–4239
DOI 10.1007/s10853-006-0663-x

Cooling rate dependent as-cast microstructure and mechanical properties of Zr-based metallic glasses

M. Yan · J. Shen · J. F. Sun · J. Zou

Received: 27 March 2006 / Accepted: 10 July 2006 / Published online: 3 March 2007

Abstract In this article, wedge chill casting is used to provide a variation of the cooling rate for the study of cooling rate-dependent as-cast microstructure and mechanical properties of Zr-based metallic glasses with and without yttrium doping. In-situ formed crystalline phases and crystallization sequence are realized in the context of the cooling rate. Macro-hardness is studied via the Brinell ball indentation and the contact morphology is discussed on the basis of microstructure analysis.

Introduction

Metallic glasses are good examples of cooling rate sensitive materials. From the first group of metallic glasses obtained under extremely high cooling rates in the 1960's [1] to modern bulk metallic glasses (BMGs) achieved via common chill casting techniques, vast types of metallic glasses have been developed and shown the cooling rate sensitivity [2, 3]. Besides its role as the determinative factor in the vitrificaiton process of BMGs, the cooling rate can also influence the crystallization products [4], the fine microstructure [5] and the physical properties [6].

However, knowledge on the cooling rate-dependent as-cast microstructure and mechanical properties of BMGs is still very limited, and more insights into these areas are undoubtedly needed. For such research incentives, techniques of wedge chill casting and the Brinell ball indentation are employed in the present study. The wedge chill casting technique is ideal for such an application due to its processed large cooling rate variation within a single alloy composition, e.g., about 2 orders in magnitude from the tip to the bottom end for BMGs with sample thickness of 10 mm [7, 8]. However, this technique was used only in very few studies [9, 10] and was employed mostly to compare the glass forming ability (GFA) between different BMG forming alloys.

Performing on a small volume of the testing material, indentation is an effective and efficient way to study the mechanical behavior of materials. It is especially useful for those not suitable to be tested in bulk forms, either due to their brittleness or bulk samples not available at all (such as the traditional metallic glasses which critical dimension was in the order of micrometer). Meanwhile, it is noticed that most existing indentation studies are conducted via sharp indenters such as Berkovich and Vickers, leaving spherical indenters like the Brinell ball ignored to a certain degree [11, 12]. However, spherical indenters have their own superiorities: (1) their sizes are the largest among indenters and accordingly can reflect the deformation behavior more macroscopically rather than just from a localized region, making them

---

M. Yan · J. Shen (✉) · J. F. Sun
School of Materials Science and Engineering,
Harbin Institute of Technology, 92 West Dazhi St.,
Harbin 150001, China
e-mail: junshen@hit.edu.cn

M. Yan · J. Zou
School Engineering and Centre for Microscopy and
Microanalysis, The University of Queensland, Brisbane,
QLD 4072, Australia

J. Zou
e-mail: j.zou@uq.edu.au

especially appropriate for the study of materials with heterogeneous microstructure and (2) they are more convenient for computer simulation [13].

In the current investigation, a recently developed Zr-based BMG [14] is selected and, for a comparative study, 0.5 at.% amount of yttrium is doped to the system as an oxygen-gettering element. Cooling rate-dependent microstructure and in-situ crystallization products are specified, and the mechanical behavior is discussed based on the microstructure analysis.

Experimental

Alloy ingots with nominal compositions of $Zr_{51}Cu_{20.7}Ni_{12}Al_{16.3}$ (referred as Zr51) and $(Zr_{0.51}Cu_{0.207}Ni_{0.12}Al_{0.163})_{99.5}Y_{0.5}$ (referred as Zr51Y0.5) were prepared by non-consumed arc melting under the protection of a high purity argon atmosphere. Wedge-shape samples were then fabricated via wedge-shape copper mould, a schematic graph of which is presented in Fig. 1. Six equally apart sections of ~6 mm each in thickness were subsequently cut from different positions of the wedge-shape samples as shown in Fig. 1 using a diamond saw. Five internal slices are then denoted as alloys A1–A5 for the Zr51 samples and B1–B5 for the Zr51Y0.5 samples, respectively. The largest difference in the cooling rate (R), i.e., between the alloys A1(B1) and A5(B5), can be estimated to be around 25 times using the Eqs. 1 and 2, suggested by Lin et al. in a Zr-based BMG [7] and by Pryds et al. in a low carbon Fe–Cr alloy [8], respectively.

$$R = 1000/d^2 (d \text{ is dimensionless value for the sample diameter which is measured in mm}) \quad (1)$$

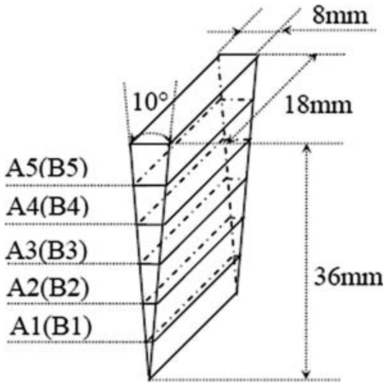

Fig. 1 Schematic graph showing the dimensions of the wedge-shape samples. Cut from the indicated positions, slices with compositions of Zr51 and Zr51Y0.5 are denoted as alloys A1–A5 and B1–B5, respectively

$$R = 962/d^2 (d \text{ is dimensionless value for the half width of the alloy slice which is measured in mm}) \quad (2)$$

A D/max IIIA X-ray diffractometer (XRD) and a Philips XL30 scanning electron microscope (SEM) were used to conduct the microstructure analysis in the present study. A JEOL 6460LV SEM was employed to perform the element mapping and to study the element distribution. XRD was operated at 40 kV and 60 mA using the Cu–K_α target. SEM was performed at 20 kV, which was equipped with the energy dispersive spectrometer (EDS) to provide the compositional information. Φ1 mm steel ball was used in the hardness test with a load of 30 kg and a holding time of 15–20 s. The hardness was determined by averaging multiple measurement results and the error limit was within 4%. The volume fraction of the crystalline phases was estimated via image analysis software and the error limit is within 10%.

Results and discussion

Microstructure analysis

The effects of the decreased cooling rates on the microstructure are illustrated by the back-scattered electron (BSE) images shown in Fig. 2a–e for the alloys A1–A5 and Fig. 2f–j for the alloys B1–B5. Specifically, a unitary *Z* contrast morphology can be seen in the alloy A1, implying a uniform amorphous structure is obtained when the cooling rate is the highest. In the alloy A2, a considerable amount of grey phases in the scale of several micrometers can be observed in the matrix, indicating that a certain degree of in-situ crystallization has taken place during the solidification process. EDS analysis of these phases detected a small amount of oxygen (over 2 at.%), which might be originated either from the raw starting materials or from the fabrication facilities. In the alloys A3–A5, additional dark dendritic phases can be seen evidently due to the decreased cooling rates. Furthermore, it is noticed that the size of the grey phase increases from several micrometers in the alloy A2 to tens of micrometers in the alloy A5, and the volume fraction increases as well. A similar tendency can also be found for the dark dendritic phases when comparing the alloys A3–A5. As such, it is suggested that other types of crystalline phases exist in the alloys A3–A5 by the EDS analysis and by careful examination of the BSE contrasts, which can also be confirmed by the subsequent XRD characterization.

Fig. 2 BSE images showing the as-cast microstructures of the alloys A1–A5 (**a**)–(**e**) and B1–B5 (**f**)–(**j**). Inserted BSE image in (**f**) shows the morphology of the yttrium oxide particle at a higher magnification

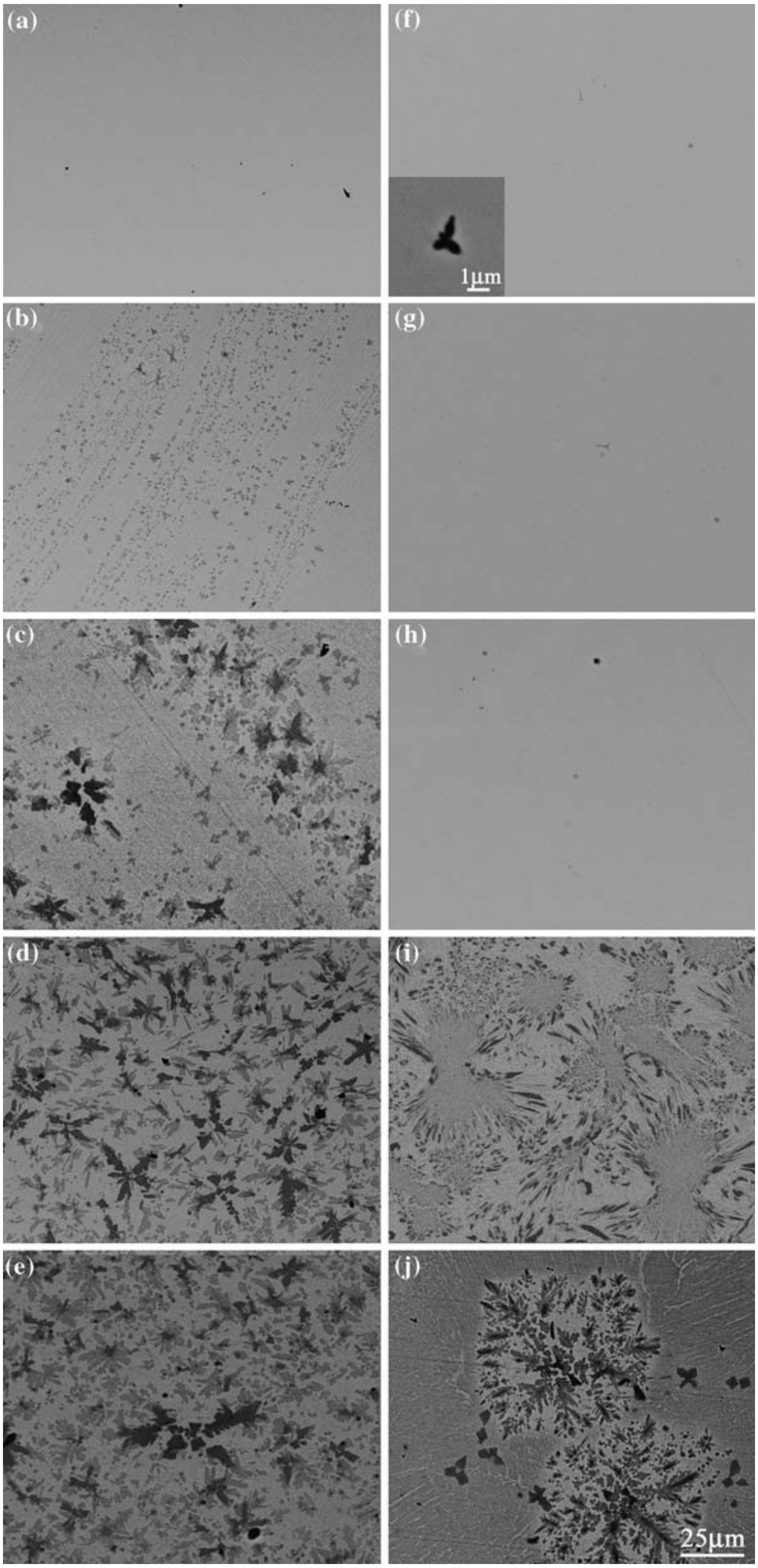

In great contrast to the undoped alloys, in-situ formed crystalline phases are only detectable in the alloys B4 and B5, leaving the alloys B1–B3 nearly featherless in the BSE images. One can also note that the morphologies of the crystalline phases visible in the alloys B4 and B5 are different from those in the alloys A4 and A5, implying that crystallization products might have changed as a consequence of the doped yttrium. Meanwhile, micrometer-scaled particles with the dark contrast can be occasionally observed in the alloys B1–B5 and they are composed of yttrium and oxygen principally as determined by the EDS analysis, suggesting the formation of yttrium oxide [see the inserted high magnification BSE image in Fig. 2f]. Regarding to the oxygen sensitivity of Zr-based BMGs [15], the greatly changed microstructures and the enhanced glass formation observed in the yttrium doped alloys are believed to be due to the formation of yttrium oxides, by which the oxygen is sucked away and its negative effect on the glass formation is consequently avoided [16].

Figure 3a and b present the XRD patterns for the alloys A1–A5 and B1–B5, respectively. Consistent with the corresponding BSE observation, the alloy A1 is shown to be in a full amorphous state as evidenced by the diffuse halo in its XRD pattern. In the alloy A2, a $NiZr_2$-type fcc structured crystal is suggested to be the primary crystalline phase, although a certain amount of Cu and Al elements can also be detected in its composition. Subsequently, four other types of crystalline phases, namely an $Al_{1.7}Ni_{0.3}Zr$-type fcc phase, a Zr_3Al_2-type tetragonal phase, an Al-riched rhombohedral phase and a Zr-riched monoclinic phase, can be identified in the alloys A3–A5 according to the XRD analysis as well as the transmission electron microscope study of the related alloys [17]. Among these crystalline phases, the fcc $NiZr_2$-type phase and the rhombohedral phase are two main phases and correspond to the above mentioned "grey phase" and "dark phase" in Fig. 2c–e, respectively.

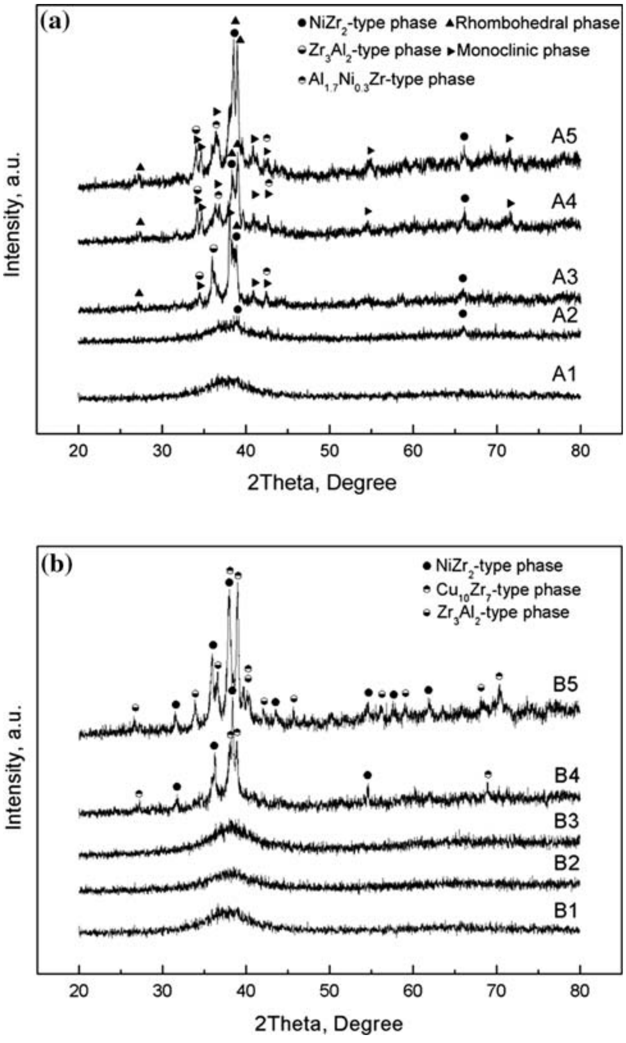

Fig. 3 XRD patterns for the alloys A1–A5 (**a**) and B1–B5 (**b**)

On the other hand, although the $NiZr_2$-type fcc structured crystal can still be determined as a crystalline phase in the alloys B4 and B5 based on the XRD results, no oxygen can be detected and the formation of yttrium oxides is believed to be the reason. Furthermore, there is another type of crystalline phase in the alloy B4 and the diffraction data suggest it being an orthorhombic structured $Cu_{10}Zr_7$ phase, which was once found in a $Zr_{55}Al_{15}Ni_{10}Cu_{20}$ BMG [18]. As the result of a further decrease in the cooling rate, Zr_3Al_2-type phase appears in the alloy B5 as the third crystalline phase, although the $NiZr_2$-type phase and the $Cu_{10}Zr_7$-type phase are still the main phases according to the XRD analysis as well as the SEM study.

Based on the above analysis, Fig. 4 shows a schematic diagram to illustrate the cooling rate-dependent in-situ crystallization sequences determined for the alloys A1–A5 and B1–B5. It can be seen that, for the

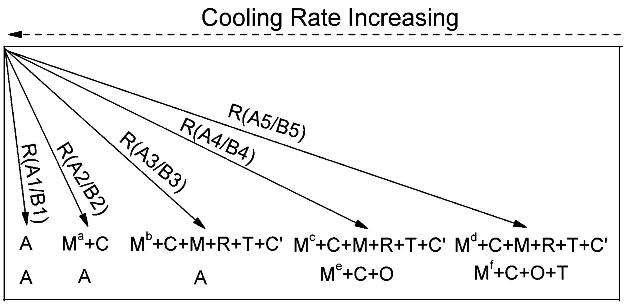

Fig. 4 Schematic graph showing the in-situ crystallization sequences for the alloys A1–A5 and B1–B5 as the consequence of the changed cooling rates. Note that as a result of the in-situ crystallization, the compositions of the matrix in these alloys are different and the superscript is accordingly used to differentiate them, such as M^a and M^b, etc. Please note that here A means "amorphous", C means "the cubic phase", M means "the monoclinic phase", R means "the rhombohedral phase" and O means "the orthorhombic phase" as mentioned in the text

alloys A1–A5, oxygen-containing/stabilized $NiZr_2$-type fcc phase is the most competitive crystalline phase, evidenced by its formation even at a higher cooling rate. As for the yttrium doped alloys B1–B5, the $Cu_{10}Zr_7$-type phase and the oxygen-free $NiZr_2$-type phase are the corresponding most active crystalline phases to compete with the amorphous structure.

In the meanwhile, a long-range element diffusion in the solidification process is expected for the slowly cooled alloys Zr51 and Zr51Y0.5, as suggested by the formation of several types of crystalline phases simultaneously in the alloys A3–A5 and B4–B5. As examples, Fig. 5a and b illustrate the element mappings of the composing elements Zr, Cu, Ni and Al for the alloys A5 and B5, which show that the intensive element diffusion is found for both alloys as evidenced by the remarkable element enrichment (with a brighter contrast) or depletion (with a darker contrast) in the BSE image. On the one hand, such a long-range diffusion indicates that the dynamic factor is significant in the in-situ crystallization process for slowly cooled Zr51 and Zr51Y0.5 alloys. On the other hand, the long-range diffusion is actually a good trace for BMG forming alloys, since in-situ crystallization in this case will be sluggish due to the required element rearrangement at a large scale [2]. This is especially true when concerning Zr and Al, as they are the largest ones in radius among the four composing elements ($r_{Zr} = 0.216$ nm, $r_{Cu} = 0.157$ nm, $r_{Ni} = 0.162$ nm and $r_{Al} = 0.182$ nm).

Mechanical behavior

Macro-hardness values obtained from the Brinell ball indentation are presented in Fig. 6a. It shows that a tendency of the lower the cooling rate, the higher the hardness is generally visible for both Zr51 and Zr51Y0.5 alloys, and the hardness values of alloys A2–A4 are a little higher than the corresponding values of alloys B2–B4, which may result from the different crystallization products incurred by the doped yttrium. In Fig. 6b, the volume fractions of the crystalline phases are plotted as a function of the cooling rate/alloy slices. In turn, the increased hardness values should be due to the enlarged volume fraction of the crystalline phases for alloys A1–A5 and B4–B5. Based on the free volume model [19, 20], it is known that the free volume will be reduced as a consequence of the increased volume fraction of the crystalline phases in BMG alloy systems. Accordingly, the plastic flow will be harder to develop considering its relationship with the free volumes and this will in turn incur higher hardness values [21]. At the same time, a noticeable increment in hardness in the alloys B1–B3 is also detected, indicating that the hardness can be changed with the cooling rates even all of the alloys are in amorphous state. Actually, a similar phenomenon was also reported in a Pd-based BMGs [6], in which the cooling rate was found to affect the density as well as the microhardness.

Furthermore, the indentation morphology is carefully examined in order to investigate the deformation behavior via the contact between the indenter and the alloys, in which several contact characteristics have been observed. One of these is the featureless contact morphology that exists in the alloys with amorphous or nearly full amorphous structure, i.e., in the alloys A1 and B1–B3. Figure 7a presents such an example detected in the alloy B1, and it can be seen that no obvious characteristics such as shear bands or pile-up/

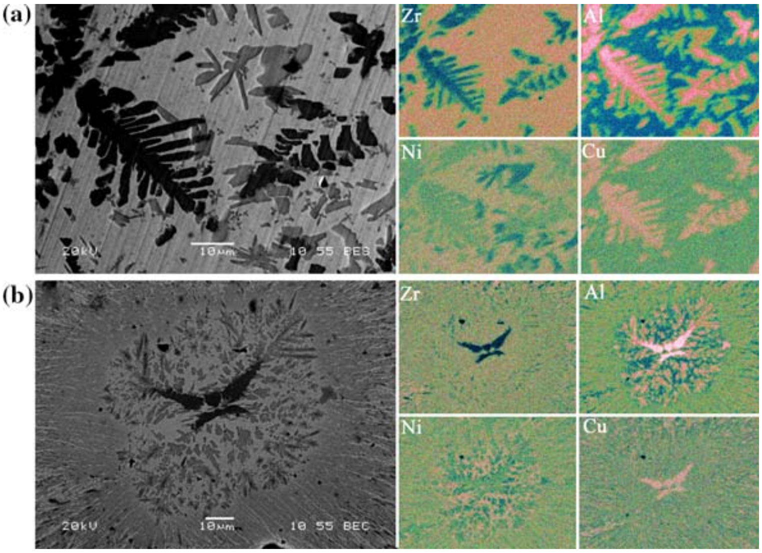

Fig. 5 BSE images for the alloys A5 (**a**) and B5 (**b**). Element mapping results of Zr, Cu, Ni and Al elements for both alloys are presented

Fig. 6 Hardness determined by the Brinell ball indentation (**a**) and the volume fractions of the crystalline phases (**b**) of the alloys A1–A5 and B1–B5

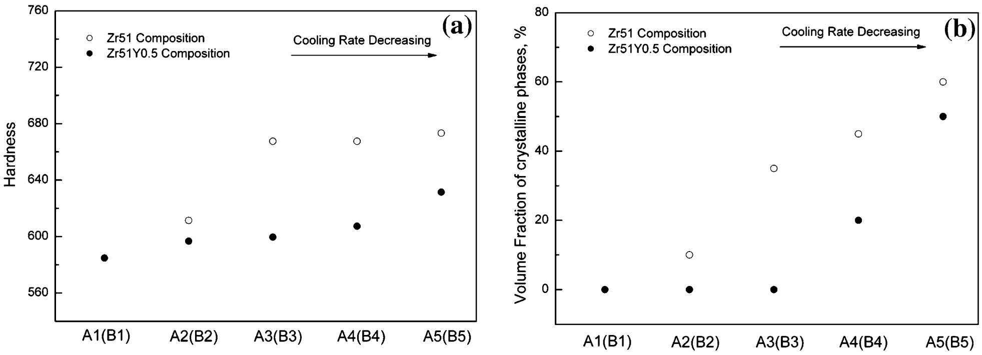

sink-in phenomenon can be observed. Limited plastic deformation ability of BMGs may be the reason for the absence of the shear bands. As such, since the pile-up/sink-in phenomenon is closely related to the strain hardening properties of materials [22], its absence might thus be due to the neglectable work hardening ability of BMGs.

Meanwhile, a large number of shear band structure can be found in the alloys that contain considerable amounts of crystalline phases, and two such cases, detected in the alloys A2 and A4, are shown in Fig. 7b and d, respectively. In Fig. 7b, shear bands can be seen to distribute across the whole inner wall of the contact area. At the same time, a pore structure can be observed in the middle of the indentation (Fig. 7c) as a further proof of the sustained intensive plastic deformation. Checking the corresponding microstructure of the alloy A2 (Fig. 2b), it is suggested that this mor-

Fig. 7 SE image presenting the indentation morphology observed in the alloy B1 (**a**), SE images showing the shear band structure and the pore structure observed in the alloy A2 (**b**) and (**c**), SE images showing the indentation morphologies observed in the alloy A4 (**d**) and (**e**) and the inserted image in (**e**) is a BSE image showing the distribution of crystalline phases, SE image showing Hertz rings and cracking phenomenon observed in the alloy A5 (**f**) with an inserted BSE image showing the in-situ formed crystalline phases

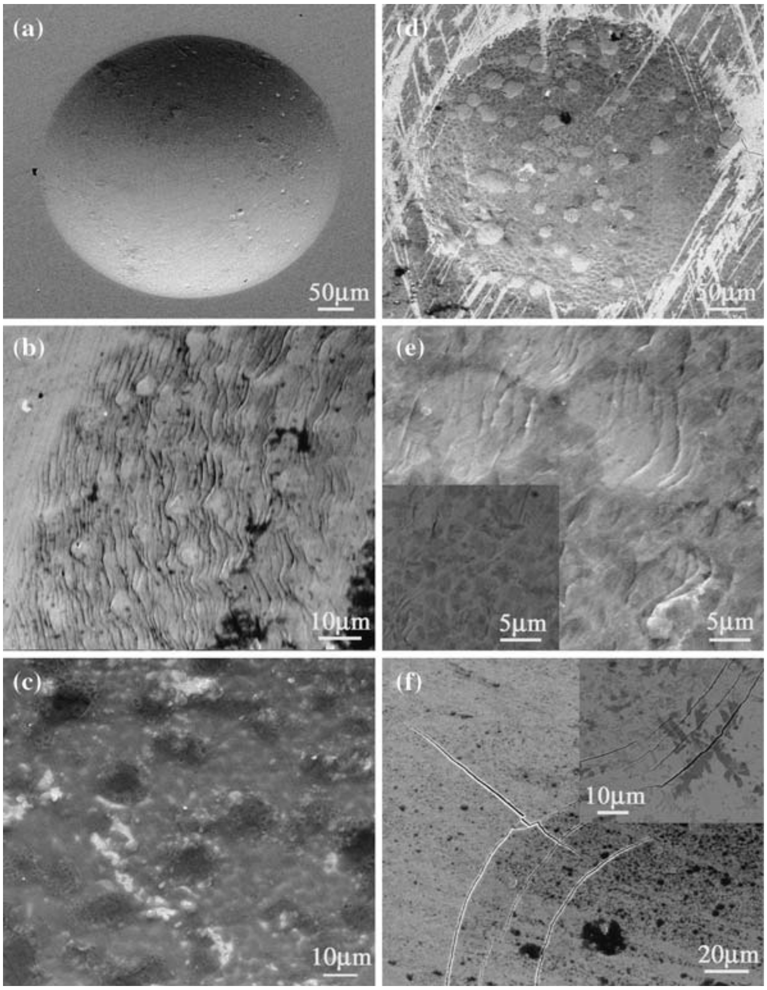

phology might result from a mixture of the amorphous matrix and the homogeneously distributed micrometer-scaled primary phases. In the meantime, Fig. 7d and e show an interesting "Lunar Crater" contact morphology that is detected in the alloy A4, which shows intensive shear band structures in each tunnel. Indicated by the inserted BSE image in Fig. 7e, evenly distributed crystalline phases might behave as the obstacles to the development of the shear process and in turn cause the multiplication of them.

It is known that limited plasticity is one weakness of metallic glasses and the plastic deformation ability of metallic glasses is directly related to shear band development, therefore the above mentioned observations of large numbers of shear bands indicate good plasticity may exist in two types of microstructures. One is a dual phase structure which has an amorphous matrix together with primary crystalline phases as the secondary phase (see Fig. 2b for the alloy A2). In this case, the crystalline phases may serve as the origins of the shear band nucleation and in turn incur shear band multiplication, performing in a way similar as some in-situ formed or extrinsic secondary phase strengthened BMG composites [23, 24]. The other contains several types of crystalline phases and their sizes are comparable to each other (see Fig. 2d for the alloy A4). For their increased volume fractions and grain sizes, these crystalline phases may block and trap shear bands in the process of deformation, and accordingly incur localized shear band structure and the multiplication of shear bands as well.

It is also noted that not all of the crystalline phase-containing alloys show the shear band multiplication morphology and, in certain cases such as in the alloys A3, A5 and B5, a tendency towards serious loss of plasticity can even be observed. Figure 7f shows such an example found in the alloy A5, in which Hertz rings can be seen and a tensile stress induced cracking appears and extends from the convergent point of the Hertz rings to the free surface. The BSE image inserted in Fig. 7f suggests that unevenly distributed crystalline phases may be the reason for such an elastic contact morphology, implying that the control of cooling rate is mandatory in order to achieve ideal microstructure and, in turn, good plasticity in the in-situ formed BMG composites [25].

Conclusions

Wedge chill casting is employed in the current study to investigate the responses to the cooling rate of two BMG forming alloys $Zr_{51}Cu_{20.7}Ni_{12}Al_{16.3}$ and $(Zr_{0.51}Cu_{0.207}Ni_{0.12}Al_{0.163})_{99.5}Y_{0.5}$ in terms of microstructure and macro-hardness. Both alloys showed cooling rate-dependent as-cast microstructure and mechanical properties. Different microstructures, from amorphous to the well-crystallized, have been observed as the result of the decreased cooling rates, from which the crystallization sequence is determined and long-range diffusion of composing elements is observed in the conditions of lowered cooling rates. In general, macro-hardness is determined to increase with the decreased cooling rates and three types of contact morphology are realized in the alloys formed at different cooling rates.

Acknowledgement This work was supported by the Program for New Century Excellent Talents in University (China).

References

1. Klement W, Willens RH, Duwez P (1960) Nature 187:869
2. Inoue A. (2000) Acta Mater 48:279
3. Johnson WL (1999) MRS Bull 24:42
4. Gebert A, Eckert J, Sculzt L (1998) Acta Mater 46:5475
5. Xing LQ, Hufnagel TC, Eckert J, Löser W, Schultz L (2000) Appl Phys Lett 77:1970
6. Hu X, Ng SC, Feng YP, Li Y (2001) Phy Rev B 64:172201
7. Lin XH, Johnson WL (1995) J Appl Phys 78:1
8. Pryds NH, Huang X (2000) Metal Mater Trans A 31:3155
9. Xing LQ, Ochin P, Harmelin M, Faudot F, Bigot J, Chevalier JP (1996) Mater Sci Eng A 220:155
10. Inoue A, Shinohara Y, Yokohama Y, Masumoto T (1995) Mater Trans JIM 36:1276
11. Schuh CA, Nieh TG (2004) J Mater Res 19:46
12. Tang CG, Li Y, Zeng KY (2004) Mater Sci Eng A 384:215
13. Patnaik MNM, Narasimhan R, Ramamurty U (2004) Acta Mater 52:3335
14. Shen J, Zou J, Ye L, Lu ZP, Xing DW, Yan M, Sun JF (2005) J Non-Cryst Solids 351:2519
15. Liu CT, Chisholm MF, Miller MK (2002) Intermetallics 10:1105
16. Yan M, Shen J, Zhang T, Zou J (2006) J Non-Cryst. Solids 352:3109
17. Yan M, Zou J, Shen J J Alloys Compd. doi: 10.1016/j.jallcom.2006.06.034
18. Zhang J, Wei YH, Qiu KQ, Zhang HF, Quan MX, Hu ZQ (2003) Mater Sci Eng A 357:386
19. Spaepen F (1977) Acta Mater 25:407
20. Steif PS, Spaepen F, Hutchinson JW (1982) Acta Mater 30:447
21. Yan M, Sun JF, Shen J (2004) J Alloys Compd 381:86
22. Field JS, Swain MV (1995) J Mater Res 10:101
23. Choi-Yim H, Koster U, Busch R, Johnson WL (1999) Acta Mater 47: 2455
24. Fan C, Ott RT, Hufnagel TC (2002) Appl Phys Lett 81:1020
25. He G, Loser W, Eckert J (2003) Acta Mater 51:5223